Subsurface Weathering Revealed in Hillslope-Integrated Porosity Distributions

Russell P. Callahan, Clifford S. Riebe, Sylvain Pasquet, Ken L. Ferrier, Dario Grana, Leonard S. Sklar, Nicholas J. Taylor, Brady A. Flinchum, Jorden L. Hayes, Bradley J. Carr, et al.

AGU ADVANCING EARTH AND SPACE SCIENCE

Geophysical Research Letters

RESEARCH LETTER
10.1029/2020GL088322

Subsurface Weathering Revealed in Hillslope-Integrated Porosity Distributions

Russell P. Callahan[1], Clifford S. Riebe[1], Sylvain Pasquet[1,2], Ken L. Ferrier[3], Dario Grana[1], Leonard S. Sklar[4], Nicholas J. Taylor[1], Brady A. Flinchum[5], Jorden L. Hayes[6], Bradley J. Carr[1], Peter C. Hartsough[7], Anthony T. O'Geen[7], and W. Steven Holbrook[8]

[1]Department of Geology and Geophysics, University of Wyoming, Laramie, WY, USA, [2]Université de Paris, Institut de Physique du Globe de Paris, CNRS, Paris, France, [3]Department of Geoscience, University of Wisconsin-Madison, Madison, WI, USA, [4]Department of Geography, Planning and Environment, Concordia University, Montreal, Quebec, Canada, [5]CSIRO Deep Earth Imaging FSP, Glen Osmond, South Australia, Australia, [6]Department of Earth Sciences, Dickinson College, Carlisle, PA, USA, [7]Department of Land, Air, and Water Resources, University of California, Davis, CA, USA, [8]Department of Geosciences, Virginia Polytechnic Institute and State University, Blacksburg, VA, USA

Key Points:
- Aggregating geophysical estimates of porosity yields a new, site-integrated perspective on subsurface weathering
- Results from the Sierra Nevada, California, highlight differences between porosity distributions inferred from cores and geophysical surveys
- This analysis illustrates the value of the site-integrated perspective obtained by aggregating geophysical data over hillslope scales

Supporting Information:
- Supporting Information S1

Correspondence to:
R. P. Callahan,
rcallaha@uwyo.edu

Citation:
Callahan, R. P., Riebe, C. S., Pasquet, S., Ferrier, K. L., Grana, D., Sklar, L. S., et al. (2020). Subsurface weathering revealed in hillslope-integrated porosity distributions. *Geophysical Research Letters*, *47*, e2020GL088322. https://doi.org/10.1029/2020GL088322

Received 13 APR 2020
Accepted 30 JUN 2020
Accepted article online 17 JUL 2020

Abstract Subsurface weathering has traditionally been measured using cores and boreholes to quantify vertical variations in weathered material properties. However, these measurements are typically available at only a few, potentially unrepresentative points on hillslopes. Geophysical surveys, conversely, span many more points and, as shown here, can be used to obtain a representative, site-integrated perspective on subsurface weathering. Our approach aggregates data from multiple seismic refraction surveys into a single frequency distribution of porosity and depth for the surveyed area. We calibrated the porosities at a site where cores are coincident with seismic refraction surveys. Modeled porosities from the survey data match measurements at the core locations but reveal a frequency distribution of porosity and depth that differs markedly from the cores. Our results highlight the value of using the site-integrated perspective obtained from the geophysical data to quantify subsurface weathering and water-holding capacity.

Plain Language Summary Weathering beneath the landscape surface breaks rock down, creating soil and opening pore space capable of storing life-sustaining water for overlying ecosystems. Here we use existing geophysical techniques to produce a new site-wide perspective on subsurface weathering. This approach aggregates geophysical estimates of subsurface properties needed to quantify porosity. We applied this approach across forested slopes in the Sierra Nevada, California, where previous studies measured porosity independently in cores extracted from the subsurface. The cores are vital in our calibration of the geophysical estimates of porosity. But they sample just a few potentially anomalous points on the landscape, compared to the much more representative 860-m length of geophysical surveys at our site. Thus, our analysis highlights the limits of core-based estimates of weathering and moreover demonstrates the value of the site-integrated perspective obtained by aggregating geophysical data over hillslope scales.

1. Introduction

Deep, subsoil weathering is fundamental to many biogeochemical, geomorphological, and hydrological processes. For example, the physical and chemical breakdown of rock at depth supports ecosystems by making rock-bound nutrients available to plants (Uhlig et al., 2017). It can also influence erosion at Earth's surface by controlling the resistance of weathered bedrock to soil production (Heimsath & Whipple, 2019) and by regulating soil particle size distributions (Marshall & Sklar, 2012), which influence river incision rates (Sklar et al., 2017) and thus set the pace of landscape evolution (Callahan et al., 2019). In addition, weathering at depth creates subsurface porosity (Navarre-Sitchler et al., 2015), which stores water and mediates groundwater recharge and discharge (Harman & Cosans, 2019), with implications for overlying ecosystems (Hahm et al., 2019).

Deep subsurface weathering, below the upper meter of soil, has traditionally been quantified by measuring chemical depletion and volumetric strain in samples from cores (Riebe et al., 2017). However, because these samples can be difficult and costly to obtain, they are typically limited in number at any given site. Moreover, even when cores are available, their small cross-sectional area necessarily samples a small fraction of the

subsurface. Therefore, they may not be spatially representative of subsurface weathering at a site. Near-surface geophysics can augment data from cores, penetrating through the weathering profile in surveys spanning 10^1–10^3-m horizontal scales (Comas et al., 2019; Parsekian et al., 2015). For example, hillslope-scale seismic refraction surveys can be used to compute seismic velocity tomograms, which represent horizontal and vertical variations in weathering (e.g., Befus et al., 2011). Slower seismic velocities generally correspond to greater subsurface weathering (Olona et al., 2010), but seismic velocities alone only provide relative measurements of weathering, unlike more direct measurements of chemical depletion and volumetric strain from cores (Hayes et al., 2019).

This obstacle can be overcome with rock physics relationships that convert seismic velocity tomograms into porosity tomograms (e.g., Holbrook et al., 2014). Subsurface porosity reflects the initial porosity of the protolith plus subsequent porosity production due to chemical depletion and volumetric strain that occur during subsurface weathering. Hence, porosity is a quantitative measure of the combined effects of chemical and physical weathering (Hayes et al., 2019). However, geophysical studies of the critical zone have not commonly used porosity to quantify weathering, instead focusing on its role in hydrology. For example, studies of how porosity varies with depth and distance along hillslope-spanning surveys have recently been used to quantify spatial patterns in water-holding capacity (e.g., Flinchum et al., 2018).

Here we show how these spatial patterns can be consolidated into a site-integrated perspective on porosity that reveals the central tendency, variance, and trend in subsurface weathering with depth. The approach aggregates estimates of porosity from multiple seismic refraction surveys into a single bivariate distribution of porosity and depth. To illustrate the power of this approach, we applied it across forested slopes in the southern Sierra Nevada, California, where subsurface porosity was quantified in previous work by measuring bulk density of cores extracted from saprolite. We used the cores to calibrate a Bayesian rock physics model of seismic refraction data and obtained a close match between observed and modeled porosities at the core locations, indicating that the rock physics model yields realistic estimates of porosity. Yet, on a site-wide basis, the geophysics-based porosities indicate that there is more water-holding capacity near the surface, less water-holding capacity at intermediate depths, and thicker soil and saprolite at many locations, relative to what can be inferred from the cores. These differences reflect the more extensive—and more representative—spatial coverage of the geophysical surveys, relative to the cores. Our analysis illustrates the value of the site-integrated perspective obtained by aggregating geophysics-based porosities over hillslope scales.

2. Study Design

To explore the use of geophysics in obtaining a site-wide perspective on subsurface weathering, we acquired cores and seismic refraction data from a ridgetop in the D102 catchment of the Southern Sierra Critical Zone Observatory, in the Sierra Nevada Batholith (Figure 1). This site is advantageous for several reasons. First, because we placed transects on a single, well-defined ridgetop, our analysis should be largely unaffected by variations in weathering that are driven by differences in landscape position (St. Clair et al., 2015). Thus, our measurements should be broadly representative of subsurface weathering under ridgetops in the area. Second, because the protolith is crystalline, initial porosity is likely less than a few percent, so that saprolite porosity is largely reflective of chemical and physical weathering. Third, D102 is near P301 (Figure 1a), where previous studies acquired cores along a seismic refraction survey (Hayes et al., 2019; Holbrook et al., 2014), thus enabling calibration of rock physics-based estimates of porosity at core locations. This calibration should be applicable at both P301 and D102, given their similar bedrock, vegetation, and climate.

3. Methods

3.1. Porosity Estimates From Geoprobe Cores

To quantify porosity and saturation independent of the new geophysical data from D102, we collected saprolite from six boreholes with 7-m maximum depth in August 2015 using a Geoprobe 6610DT (Figure 1b). Push cores were collected in 1-m increments using 3-cm-diameter plastic sleeves sealed with vinyl caps and parafilm to prevent moisture loss. Samples were weighed before and after drying for 24 hr at 105°C to obtain wet and dry material mass and volumetric water content. Bulk density was calculated as dry mass divided by

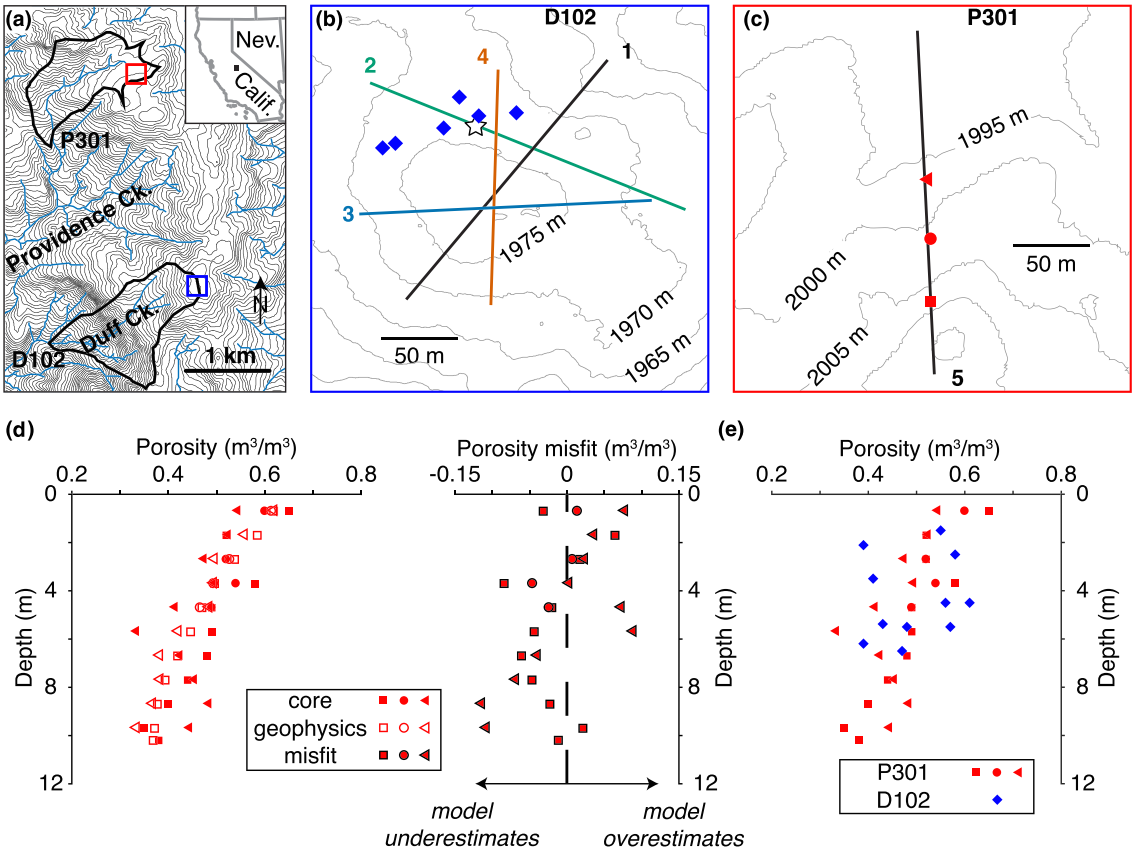

Figure 1. (a) Study location in California (inset) and map of P301 and D102 catchments (thick lines) showing 10-m elevation contours, streams (cyan), and study sites shown in (b) and (c). The area was not glaciated in the Pleistocene and has a Mediterranean climate with a 9°C mean annual temperature, a 1,030-mm/yr average annual precipitation rate (PRISM Climate Group, 2019), and a mixed-conifer and oak forest. (b and c) Geophysical transects (colored lines), core locations (colored symbols), and 5-m elevation contours at D102 and P301. (d) Porosities from cores (closed symbols) were used to calibrate rock physics inversion of geophysical data at Geoprobe locations in P301. Open symbols show best fit model (left). Misfit between predictions and observations for best fit model are scattered around dashed line showing perfect agreement (right). (e) Porosities from cores at D102 (blue) and P301 (red).

volume for each 1-m core section, thus correcting for any compaction during push coring. Calculated bulk density was then used to estimate porosity assuming an average mineral density of 2.65 g cm^{-3}. Saturation was calculated as volumetric water content divided by porosity. One measurement of saprolite thickness was acquired along Line 2 in July 2019 by mechanized augering using a Geoprobe 7822DT. None of the cores at D102 were coincident with the geophysical surveys.

3.2. Seismic Refraction Surveys

We acquired seismic refraction data on four crossing transects spanning a ~40,000-m^2 ridgetop plot at the D102 study site during the summer of 2016 (Figure 1b). On each transect, data were collected using four Geometrics Geodes connected to ninety-six 40-Hz vertical-component geophones. Lines 1 and 2 were 238 m long with a 2.5-m geophone spacing. Lines 3 and 4 were 190 m long with a 2-m geophone spacing. Seismic energy was generated by striking a metal plate with a 12-pound sledgehammer at 10-m increments along each transect. At each position, we stacked data from five hammer blows to increase signal-to-noise ratios.

We estimated subsurface compressional (P) wave velocity (V_P) structure by manually identifying first arrival times of the seismic energy at each geophone. This yields a P wave travel time for each shot-receiver combination. We then used a least squares ray tracing code (St. Clair, 2015) to convert travel times into a tomogram of V_P along each transect (Figures 2a–2d). To calculate the average and standard deviation of V_P for the porosity calculations, we repeated the tomogram calculations 50 times for each transect using initial models

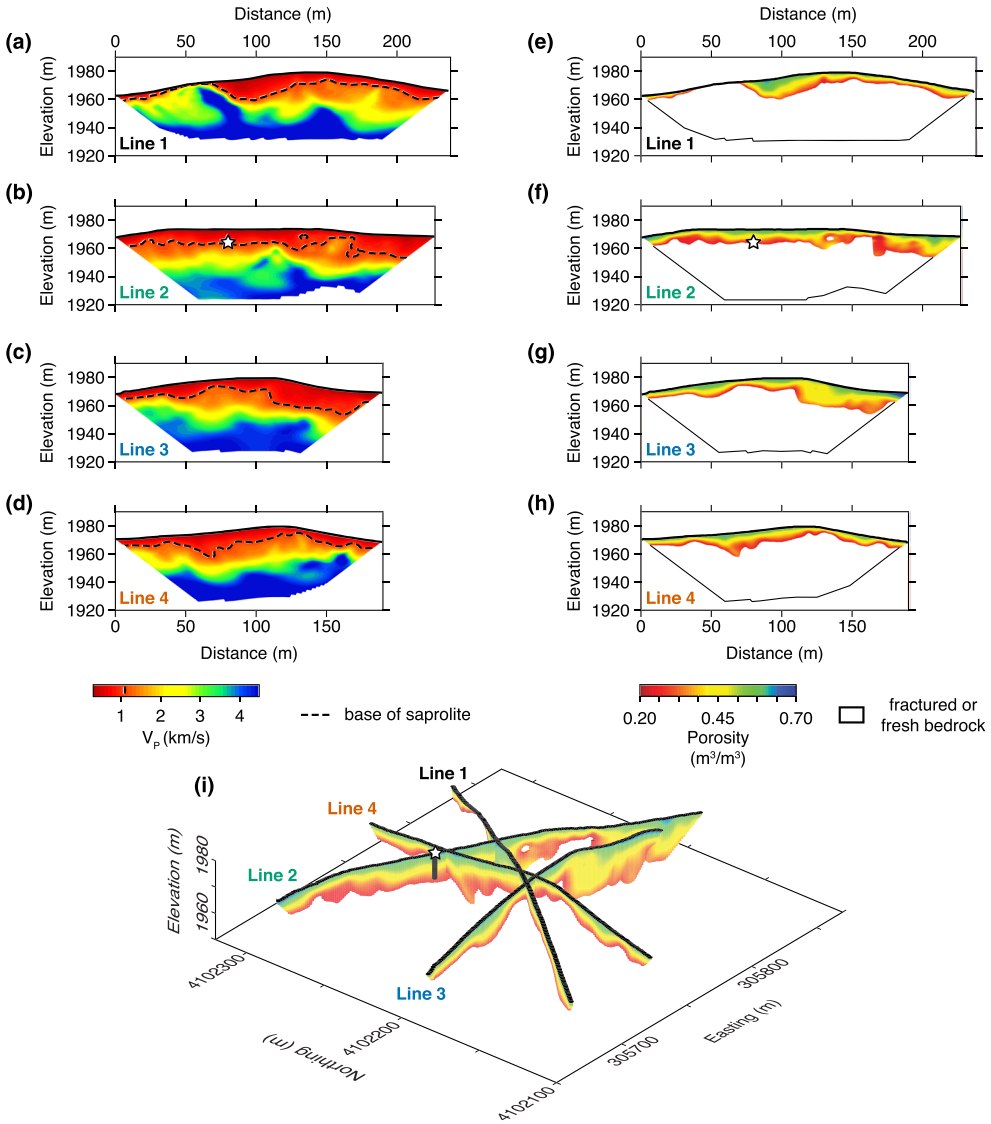

Figure 2. *P* wave velocity (a–d) and inferred saprolite porosity (e–h) reveal variations in weathering across each transect. Distance = 0 m for each survey at corresponding label on fence diagram (i). Dashed lines (a–d) mark 1.1-km s^{-1} V_P threshold that defines base of saprolite, a choice corroborated by saprolite thickness at mechanized augering site on Line 2 (star in b, f, and i). White space between saprolite and tomogram outline (e–h) is fractured or fresh bedrock, which are not represented in rock physics model.

generated randomly from a 350- to 600-m s^{-1} range in surface velocity and a 50- to 300-m s^{-1} m^{-1} range in vertical velocity gradient.

3.3. Porosity From Rock Physics Modeling

To predict porosity from V_P, we used a rock physics model that interpolates between two endmember conditions: unaltered bedrock with zero porosity and a matrix of interconnected spherical grains at a critical porosity (φ_{crit}) that defines the threshold of suspension (Dvorkin & Nur, 1996). The rock physics model is an idealized geometric description derived to represent porosity in reservoir rocks (e.g., Dvorkin & Nur, 1996), and it remains unknown whether it represents critical zone porosity mechanistically. Irrespective of whether or not it is mechanistic, recent studies at sites with granitic saprolite similar to D102 indicate it yields realistic predictions (e.g., Hayes et al., 2019).

Our rock physics modeling closely followed the approach used in those studies (e.g., Flinchum et al., 2018). First, we estimated the elastic modulus of the solid phase using a Voight-Reuss-Hill average for the assumed mineralogy. Next, we used Hertz-Mindlin contact theory and Hashin-Shtrikman elastic bounds to estimate the bulk and shear moduli of the saprolite, accounting for water using Gassmann's equation (Hayes et al., 2019), with water content estimated from the cores (Figure S1a in the supporting information). The resulting estimates of physical properties were used to calculate *P* wave velocities over a range in porosity and saturation. Finally, we predicted porosity from V_P by solving a Bayesian inverse problem (Grana, 2016) using porosities from the cores to define both the prior porosity distribution and the change in overburden pressure with depth. We point readers to Holbrook et al. (2014) for the rock physics formulas and Tables S1 and S2 for a complete list of model parameters, including mineralogy and variables constrained by previous studies (Dahlgren et al., 1997; Mavko et al., 2009).

The rock physics model requires estimates of φ_{crit} and the average contact number (N)—that is, the number of points of contact between grains—which are commonly adopted from the literature. However, to our knowledge, no measurements of φ_{crit} and N are available for granitic saprolite, because rock physics modeling is new in critical zone research. Hence, we used a calibration approach, quantifying the best fit values of φ_{crit} and N by minimizing the sum-of-squared misfits between modeled and observed porosities at the core locations in P301 (Figures 1d and S2b). We explored a 0.30- to 0.45-m^3/m^3 range in φ_{crit} and a 5–14 range in N and found the lowest sum-of-squared misfits at $\varphi_{crit} = 0.37$ m^3/m^3 and $N = 14$ (Figure S2a), which are within the range of literature values for reservoir rocks (Mavko et al., 2009; Nur et al., 1998). Although the misfits are all less than ± 0.12 m^3/m^3, they vary systematically with depth (Figure 1d), raising the possibility that rock physics parameters are not uniform with depth, contrary to our assumptions. However, the systematic misfit does not disappear when we relax these assumptions and vary mineralogy with depth (Figure S3a), suggesting that any effect of varying mineralogy is small enough to ignore.

4. Results

4.1. Saprolite Thickness and Porosity

Measurements from the cores show overlap between D102 and P301 in their porosity-versus-depth relationships (Figure 1e), consistent with an upward increase in subsurface weathering at both sites. This overlap may reflect the similar bedrock, climate, and vegetation of the sites (Hahm et al., 2014) and moreover supports using the φ_{crit} and N calibrated at P301 in the rock physics inversions of the V_P tomograms from D102.

The depth of investigation for V_P extends below the 4-km s^{-1} contour (Figures 2a–2d), which defines the top of bedrock according to previous work at P301 (Holbrook et al., 2014). Thus, the V_P tomograms include soil, saprolite, and both fractured and fresh bedrock. Because our goal was to quantify porosity in soil and saprolite (Figures 2e–2h), where most chemical weathering occurs (e.g., White et al., 1998) and where most plant-accessible water is stored under mountain slopes in the region (Klos et al., 2018), it was important to separate soil and saprolite from fractured and fresh bedrock in our analysis.

We identified soil and saprolite as material with $V_P < 1.1$ km s^{-1}, the average velocity at the base of granitic saprolite in 13 boreholes examined in previous work (Flinchum et al., 2018). This yields estimates of saprolite thickness that are internally consistent across our site: At the five points where geophysical transects cross (Figure 2i), the depth of the 1.1-km s^{-1} contour differs by 0.6, 1.2, 1.6, 2.2, and 3.0 m between transects. Similarly, saprolite thickness predicted from the 1.1-km s^{-1} contour is just 1.5 m thicker than observed at the location on Line 2 where we measured it by mechanical augering (Figure 2b,i). These differences are similar to approximate estimates of tomogram resolution (Zelt et al., 2006), which varies from ~2–2.5 m at the surface (the geophone spacing) to ~3–7 m at $V_P = 1.1$ km s^{-1} (the base of saprolite) for a source frequency of 50–100 Hz (generated by a sledge hammer). This indicates that $V_P = 1.1$ km s^{-1} accurately identifies the base of saprolite. The inferred lateral variations in saprolite thickness (Figures 2e–2h) are consistent with what we observe in roadcuts in the region.

The soil and saprolite together span a fraction of the investigation depth of the surveys (Figures 2e–2h) but have high water-holding capacity, with porosity increasing from 0.2 m^3/m^3 at depth to ~0.7 m^3/m^3 near the surface. Because the transects cross at multiple locations, they yield a three-dimensional map of spatial variations in subsurface porosity and thus saprolite weathering across the D102 ridgetop (Figure 2i).

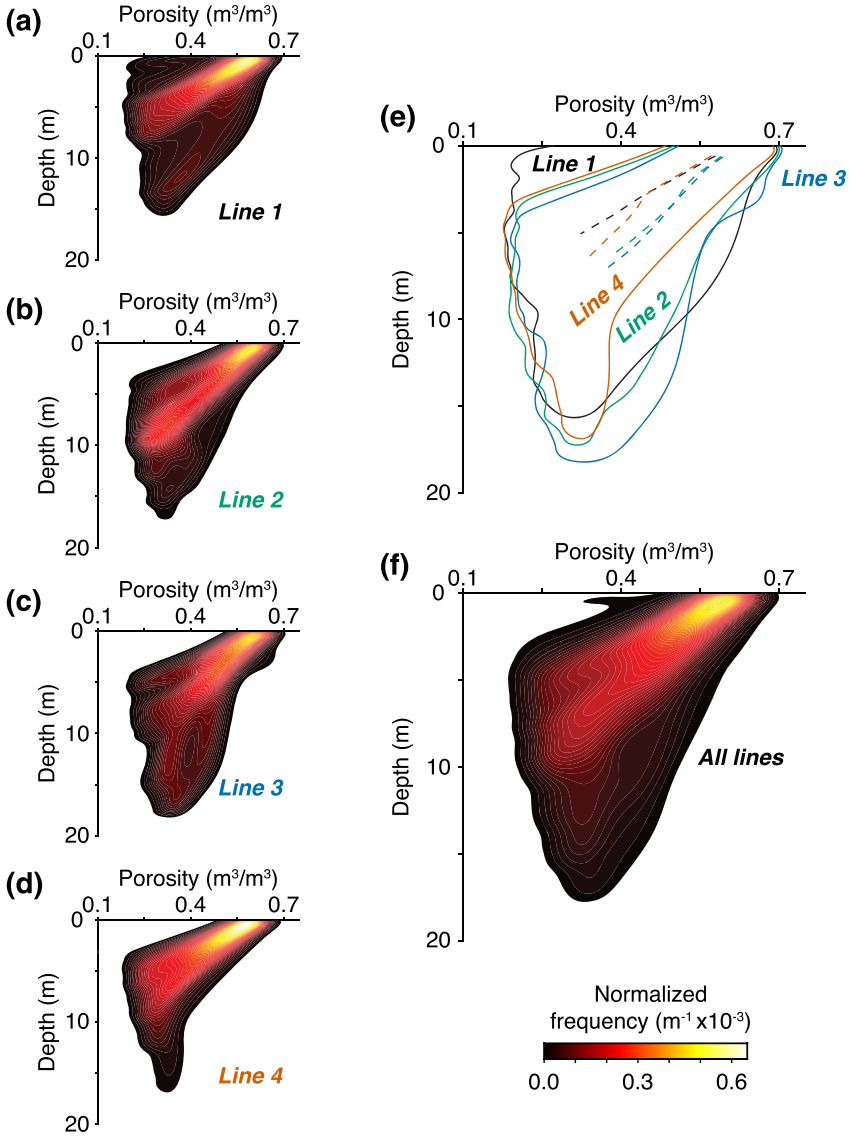

Figure 3. (a–d) Distributions of porosity and depth for transects at D102, computed by consolidating along-slope variations in porosity from each transect (Figures 2e–2h) and plotted using ksdensity function in MATLAB. (e) Outlines (solid) and modal trends (dashed) of porosity versus depth from (a)–(d). (f) Joint distribution of porosity and depth for all transects combined.

4.2. Bivariate Distributions of Subsurface Porosity and Depth

For an integrated perspective on the porosity-versus-depth relationship on each transect, we collapsed the lateral variability from each porosity tomogram (Figures 2e–2h) into a transect-wide representation of how porosity varies with depth (Figures 3a–3d). Each transect-wide porosity distribution contains many estimates from the tomogram and should therefore be spatially representative of the central tendency, variance, and gradient with depth along each transect. The bivariate frequency distributions closely overlap (Figure 3e), despite transect-to-transect differences in the porosity tomograms (Figures 2e–2h), transect orientation (Figure 2i), and any seismic wave anisotropy that may exist in the subsurface (Novitsky et al., 2018). This suggests that subsurface weathering does not differ substantially between transects. All transects have the same modal porosity of roughly 0.65 m^3/m^3at the surface, and it decreases with depth at a similar rate in each case, to roughly 0.3 m^3/m^3 at 6- to 8-m depth (Figure 3e). Given the close

agreement among the distributions, we combined them together into a single distribution that quantifies the central tendency, range, and gradient in subsurface weathering with depth across the ridgetop plot spanned by the transects (Figure 3f).

5. Discussion

5.1. Quantifying Subsurface Weathering From Porosity Distributions

Uncertainties in geophysics-based porosity estimates can arise from several sources, including V_P from the travel time inversions, estimated here to have a relative standard deviation of 2% in saprolite based on the different starting models. This variability is propagated through the rock physics model, which has additional uncertainties from the prior porosity distribution and from assumptions about the velocity-porosity relationship, leading to an overall uncertainty of 3–5% in the individual estimates of porosity. Uncertainty in saturation causes less than $\pm$0.025-m^3/m^3 uncertainty in porosity across a 0–90% range in saturation (Figure S1b), which is higher than the likely difference in saturation between 2015 during core sampling and 2016 during geophysical data acquisition, indicating that the difference in sampling date is not a confounding factor in our analysis. Similarly, uncertainties in mineralogy were shown in a previous work to have minimal effect on porosity at P301 (Holbrook et al., 2014), and this is likely true at D102 as well, given its similar lithology. One additional source of uncertainty for some of the data is the extrapolation of the rock physics model to porosities less than 0.33 m^3/m^3, the minimum observed in cores, which was necessary because none of the cores extended to the base of saprolite. However, only 2.5% of the data have predicted porosities lower than 0.25 m^3/m^3, at values that are far from the calibrated range. In addition, the lowest porosities of ~0.20 m^3/m^3 at the base of saprolite are consistent with basal saprolite porosities in other granitic terrain (Krank & Watters, 1983). Moreover, the rock physics model is nearly linear in velocity and porosity over a porosity range of 0.2–0.33 m^3/m^3 (Flinchum et al., 2018). Therefore, errors introduced by the extrapolation are expected to be small. Irrespective of the overall uncertainty, the match between the geophysics and the calibration data (Figure 1d) indicates that the rock physics model yields realistic estimates of how porosity changes with depth. And because the ~860-m total length of crossing transects at D102 is confined within a 200 × 200-m area, the geophysical data should be spatially representative of variations in saprolite porosity (Figure 2i). Hence, the bivariate frequency distribution in Figure 3f should provide a robust, site-integrated perspective on subsurface weathering.

5.2. The Value of Bivariate Distributions of Porosity and Depth

To compare the site-wide perspective from geophysics (Figure 3f) with a site-wide perspective from the cores, we applied the same kernel smoothing function to the geophysics- and core-based porosities and calculated the difference between the resulting distributions (Figures 4a–4c). We found that the cores misrepresent the site-wide distribution of subsurface weathering at D102 in three ways: (i) high near-surface porosities are underrepresented by the cores, (ii) the cores overrepresent high porosities and underrepresent low porosities at intermediate depths, and (iii) low porosities at depth are not represented at all, because no cores reached the base of saprolite. Differences such as these can arise because the cores sample the subsurface at only a few points (which introduces random error due to undersampling) and are unable to represent the porosity of any unweathered, low-porosity "corestones" that might be present in the saprolite (which introduces a systematic bias toward higher porosities). In contrast, geophysics spans many locations and includes effects of both weathered saprolite and any corestones in the estimate of velocity and thus porosity. Thus, geophysics may often provide a more representative site-integrated perspective on subsurface porosity and weathering. Although the cores are useful for quantifying porosity profiles at individual points and were vital in calibrating the rock physics model at our site, the mismatch in Figure 4c indicates that cores can misrepresent subsurface weathering on a site-wide basis.

5.3. Implications for Ecosystem Water Availability

The differences between the core- and the geophysics-based porosities are also evident in profiles of water-holding capacity derived from each measurement type (Figures 4d). These profiles are calculated as

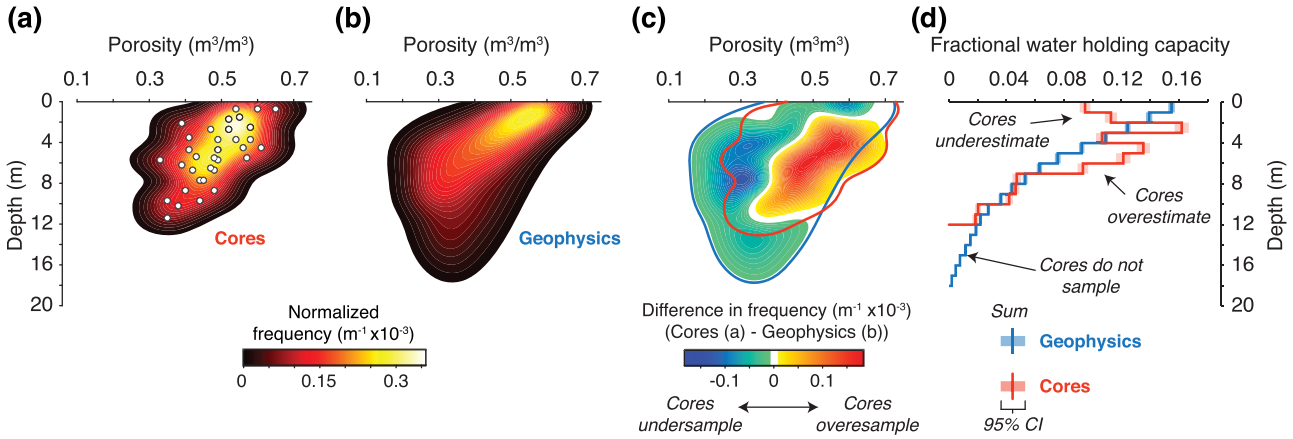

Figure 4. (a) Smoothed distribution of porosity and depth inferred from P301 and D102 cores (open circles, from Figure 1e). (b) Distribution of porosity and depth from rock physics model smoothed with same binning as (a). (c) Difference between (a) and (b) showing porosities and depths that are overrepresented and underrepresented by the limited perspective of the cores, with outlines (bold) of distributions in (a) and (b). (d) Vertical profiles of water-holding capacity from cores (red) and geophysics (blue), showing fraction of site-integrated water-holding capacity in each depth interval. Uncertainties (shaded) calculated via bootstrapping as 95% confidence intervals ("CI") using maximum misfit of ±0.12 m^3/m^3 from Figure 1d for geophysics data and an estimated analytical error of ±0.02 m^3/m^3 for the cores. Where errors do not overlap, water-holding capacity from the cores is either overestimated or underestimated.

the fraction of the site-integrated saprolite water-holding capacity in 1-m-depth increments $F_{whc,z}$ using Equation 1.

$$F_{whc,\,z} = \frac{\sum\limits_{i \,\in\, I_z} \varphi_i}{\sum\limits_{i} \varphi_i} \tag{1}$$

Here I_z is the index set of integers corresponding to porosity values that fall within the depth bin z. Hence, $F_{whc,z}$ is the sum of all porosity values in each depth interval divided by the sum of porosity values across all depths in saprolite. We applied Equation 1 to data from both the cores and the geophysics to estimate for both techniques the vertical distribution of void space and thus the amount of water that can be stored at each depth relative to the total saprolite water-holding capacity integrated across the site.

Both the cores and the geophysics show declines in $F_{whc,z}$ with depth (Figure 4d). Yet more than half of the estimated water-holding capacity occurs below 3 m, consistent with increasing recognition of the importance of deep water storage in mountain landscapes (e.g., Dawson et al., 2020). However, the core-based profile underpredicts water-holding capacity in the top 2 m and overpredicts it in the 4- to 7-m-depth range (Figure 4d). These differences cannot be explained by systematic differences in mineralogy or organic mineral content with depth (Figure S3b). Mismatches near the base of the profile occur because no cores penetrate that deeply (Figure 4d). The near-surface mismatches (Figure 4f) may have particularly important implications for understanding connections between weathering and ecosystem productivity: The cores fail to predict water-holding capacity at depths where roots are commonly abundant (Brantley et al., 2017) and therefore where water may be most needed by the ecosystem.

6. Conclusions

Our study demonstrates the value of aggregating geophysical data obtained using established techniques into a new, site-integrated perspective on subsurface porosity that quantifies weathering over hillslope scales. Rather than interpreting along-slope variations from subsurface tomograms—the traditional approach in geophysical studies of the critical zone—we consolidate data from multiple crossing surveys into a single weathering profile that quantifies the central tendency, variance, and gradient in porosity with depth for the collection of surveys. We applied this approach in the Sierra Nevada, California, where previous studies quantified porosity directly from subsurface cores. Porosities from the geophysics and the cores match at the core locations. On a site-wide basis, however, the geophysical surveys reveal more

water-holding capacity near the surface, less water-holding capacity at intermediate depths, and thicker soil and saprolite at many locations, relative to what can be seen in the cores. These discrepancies, which may have implications for understanding linkages between subsurface weathering and overlying ecosystems, reflect the more extensive—and thus more representative—spatial coverage of the geophysical surveys, relative to the cores. Our analysis demonstrates the value of aggregating geophysical data across multiple surveys to obtain a representative site-integrated perspective on subsurface weathering.

Data Availability Statement

Data from this study are available on the Mountain Scholar repository (https://doi.org/10.15786/20.500.11919/7140).

Acknowledgments

We thank Alec Spears, Troy Covill, Erin Stacy, and Megan Thompson-Munson for field assistance. Callahan acknowledges support from the Roy J. Shlemon Center for Quaternary Studies at the University of Wyoming and the Wyoming NASA Space Grant Consortium (NASA Grant NNX15AI08H). Riebe acknowledges support from National Science Foundation (NSF) Grant EAR 1331939. Holbrook acknowledges support from NSF Grant EPS 1208909.

References

Befus, K. M., Sheehan, A. F., Leopold, M., Anderson, S. P., & Anderson, R. S. (2011). Seismic constraints on critical zone architecture, Boulder Creek Watershed, Front Range, Colorado. *Vadose Zone Journal*, *10*(3), 915–927. https://doi.org/10.2136/vzj2010.0108

Brantley, S. L., Eissenstat, D. M., Marshall, J. A., Godsey, S. E., Balogh-Brunstad, Z., Karwan, D. L., et al. (2017). Reviews and syntheses: On the roles trees play in building and plumbing the critical zone. *Biogeosciences*, *14*(22), 5115–5142. https://doi.org/10.5194/bg-14-5115-2017

Callahan, R. P., Ferrier, K. L., Dixon, J., Dosseto, A., Hahm, W. J., Jessup, B. S., et al. (2019). Arrested development: Erosional equilibrium in the southern Sierra Nevada, California, maintained by feedbacks between channel incision and hillslope sediment production. *GSA Bulletin*, *131*(7–8), 1179–1202. https://doi.org/10.1130/B35006.1

Comas, X., Wright, W., Hynek, S. A., Fletcher, R. C., & Brantley, S. L. (2019). Understanding fracture distribution and its relation to knickpoint evolution in the Rio Icacos watershed (Luquillo Critical Zone Observatory, Puerto Rico) using landscape-scale hydrogeophysics. *Earth Surface Processes and Landforms*, *44*(4), 877–885. https://doi.org/10.1002/esp.4540

Dahlgren, R. A., Boettinger, J. L., Huntington, G. L., & Amundson, R. G. (1997). Soil development along an elevational transect in the western Sierra Nevada, California. *Geoderma*, *78*(3–4), 207–236. https://doi.org/10.1016/S0016-7061(97)00034-7

Dawson, T. E., Hahm, W. J., & Crutchfield-Peters, K. (2020). Digging deeper: What the critical zone perspective adds to the study of plant ecophysiology. *The New Phytologist*, *226*(3), 666–671. https://doi.org/10.1111/nph.16410

Dvorkin, J., & Nur, A. (1996). Elasticity of high-porosity sandstones: Theory for two North Sea data sets. *Geophysics*, *61*(5), 1363–1370. https://doi.org/10.1190/1.1444059

Flinchum, B. A., Holbrook, W. S., Grana, D., Parsekian, A. D., Carr, B. J., Hayes, J. L., & Jiao, J. (2018). Estimating the water holding capacity of the critical zone using near-surface geophysics. *Hydrological Processes*, *32*(22), 3308–3326. https://doi.org/10.1002/hyp.13260

Grana, D. (2016). Bayesian linearized rock-physics inversion. *Geophysics*, *81*(6), D625–D641. https://doi.org/10.1190/geo2016-0161.1

Hahm, W. J., Dralle, D. N., Rempe, D. M., Bryk, A. B., Thompson, S. E., Dawson, T. E., & Dietrich, W. E. (2019). Low subsurface water storage capacity relative to annual rainfall decouples Mediterranean plant productivity and water use from rainfall variability. *Geophysical Research Letters*, *46*, 6544–6553. https://doi.org/10.1029/2019GL083294

Hahm, W. J., Riebe, C. S., Lukens, C. E., & Araki, S. (2014). Bedrock composition regulates mountain ecosystems and landscape evolution. *Proceedings of the National Academy of Sciences of the United States of America*, *111*(9), 3338–3343. https://doi.org/10.1073/pnas.1315667111

Harman, C. J., & Cosans, C. L. (2019). A low-dimensional model of bedrock weathering and lateral flow coevolution in hillslopes: 2. Controls on weathering and permeability profiles, drainage hydraulics, and solute export pathways. *Hydrological Processes*, *33*(8), 1168–1190. https://doi.org/10.1002/hyp.13385

Hayes, J. L., Riebe, C. S., Holbrook, W. S., Flinchum, B. A., Hartsough, P. C. (2019). Porosity production in weathered rock: Where volumetric strain dominates over chemical mass loss. *Science Advances*, *5*(9), eaao0834. https://doi.org/10.1126/sciadv.aao0834

Heimsath, A. M., & Whipple, K. X. (2019). Strength matters: Resisting erosion across upland landscapes. *Earth Surface Processes and Landforms*, *44*(9), 1748–1754. https://doi.org/10.1002/esp.4609

Holbrook, W. S., Riebe, C. S., Elwaseif, M., Hayes, J. L., Basler-Reeder, K., Harry, D. L., et al. (2014). Geophysical constraints on deep weathering and water storage potential in the Southern Sierra Critical Zone Observatory. *Earth Surface Processes and Landforms*, *39*(3), 366–380. https://doi.org/10.1002/esp.3502

Klos, P. Z., Goulden, M. L., Riebe, C. S., Tague, C. L., O'Geen, A. T., Flinchum, B. A., et al. (2018). Subsurface plant-accessible water in mountain ecosystems with a Mediterranean climate. *Wiley Interdisciplinary Reviews Water*, *5*(3), e1277. https://doi.org/10.1002/wat2.1277

Krank, K. D., & Watters, R. J. (1983). Geotechnical properties of weathered Sierra Nevada granodiorite. *Environmental & Engineering Geoscience*, *xx*(2), 173–184. https://doi.org/10.2113/gseegeosci.xx.2.173

Marshall, J. A., & Sklar, L. S. (2012). Mining soil databases for landscape-scale patterns in the abundance and size distribution of hillslope rock fragments. *Earth Surface Processes and Landforms*, *37*(3), 287–300. https://doi.org/10.1002/esp.2241

Mavko, G., Mukerji, T., & Dvorkin, J. (2009). *The rock physics handbook: Tools for seismic analysis of porous media*. Cambridge: Cambridge University Press. https://doi.org/10.1017/CBO9780511626753

Navarre-Sitchler, A., Brantley, S. L., & Rother, G. (2015). How porosity increases during incipient weathering of crystalline silicate rocks. *Reviews in Mineralogy and Geochemistry*, *80*(1), 331–354. https://doi.org/10.2138/rmg.2015.80.10

Novitsky, C. G., Holbrook, W. S., Carr, B. J., Pasquet, S., Okaya, D., & Flinchum, B. A. (2018). Mapping inherited fractures in the critical zone using seismic anisotropy from circular surveys. *Geophysical Research Letters*, *45*, 3126–3135. https://doi.org/10.1002/2017GL075976

Nur, A., Mavko, G., Dvorkin, J., & Galmudi, D. (1998). Critical porosity: A key to relating physical properties to porosity in rocks. *The Leading Edge*, *17*(3), 357–362. https://doi.org/10.1190/1.1437977

Olona, J., Pulgar, J. A., Fernández-Viejo, G., López-Fernández, C., & González-Cortina, J. M. (2010). Weathering variations in a granitic massif and related geotechnical properties through seismic and electrical resistivity methods. *Near Surface Geophysics*, *8*(6), 585–599. https://doi.org/10.3997/1873-0604.2010043

Parsekian, A. D., Singha, K., Minsley, B. J., Holbrook, W. S., & Slater, L. (2015). Multiscale geophysical imaging of the critical zone. *Reviews of Geophysics*, *53*, 1–26. https://doi.org/10.1002/2014RG000465

PRISM Climate Group. (2019). PRISM Climate Data. Oregon State University.

Riebe, C. S., Hahm, W. J., & Brantley, S. L. (2017). Controls on deep critical zone architecture: A historical review and four testable hypotheses. *Earth Surface Processes and Landforms*, *42*(1), 128–156. https://doi.org/10.1002/esp.4052/full

Sklar, L. S., Riebe, C. S., Marshall, J. A., Genetti, J., Leclere, S., Lukens, C. L., & Merces, V. (2017). The problem of predicting the size distribution of sediment supplied by hillslopes to rivers. *Geomorphology*, *277*, 31–49. https://doi.org/10.1016/j.geomorph.2016.05.005

St. Clair, J. (2015). Geophysical investigations of underplating at the Middle American Trench, weathering in the critical zone, and snow water equivalent in seasonal snow. University of Wyoming.

St. Clair, J., Moon, S., Holbrook, W. S., Perron, J. T., Riebe, C. S., Martel, S. J., et al. (2015). Geophysical imaging reveals topographic stress control of bedrock weathering. *Science*, *350*(6260), 534–538. https://doi.org/10.1126/science.aab2210

Uhlig, D., Schuessler, J. A., Bouchez, J., Dixon, J. L., & Von Blanckenburg, F. (2017). Quantifying nutrient uptake as driver of rock weathering in forest ecosystems by magnesium stable isotopes. *Biogeosciences*, *14*(12), 3111–3128. https://doi.org/10.5194/bg-14-3111-2017

White, A. F., Blum, A. E., Schulz, M. S., Vivit, D. V., Stonestrom, D. A., Larsen, M., et al. (1998). Chemical weathering in a tropical watershed, Luquillo Mountains, Puerto Rico: I. Long-term versus short-term weathering fluxes. *Geochimica et Cosmochimica Acta*, *62*(2), 209–226. https://doi.org/10.1016/S0016-7037(97)00335-9

Zelt, C. A., Azaria, A., & Levander, A. (2006). 3D seismic refraction traveltime tomography at a groundwater contamination site. *Geophysics*, *71*(5), H67–H78. https://doi.org/10.1190/1.2258094